Biomaterials 236 (2020) 119805

Contents lists available at ScienceDirect

Biomaterials

journal homepage: www.elsevier.com/locate/biomaterials

In vivo assessment of tumour associated macrophages in murine melanoma obtained by low-field relaxometry in the presence of iron oxide particles

Simona Baroni[a,1], Maria Rosaria Ruggiero[a,1], Valeria Bitonto[a], Lionel M. Broche[b], David J. Lurie[b], Silvio Aime[a,c], Simonetta Geninatti Crich[a,*]

[a] Department of Molecular Biotechnology and Health Sciences, University of Torino, Via Nizza 52, Torino, Italy
[b] Aberdeen Biomedical Imaging Centre, University of Aberdeen, Foresterhill, AB25 2ZD, Aberdeen, UK
[c] Istituto di Biostrutture e Bioimmagini (IBB), CNR, Torino, Italy

ARTICLE INFO

Keywords:
Iron oxide particles
Low field relaxometry (NMRD)
Intracellular water lifetime
Tumour associated macrophages
Magnetic resonance imaging

ABSTRACT

Tumour-associated macrophages (TAM) are forced by cancer cells to adopt an anti-inflammatory phenotype and secrete factors to promote tumour invasion thus being responsible for poor patient outcome. The aim of this study is to develop a clinically applicable, non-invasive method to obtain a quantitative TAM detection in tumour tissue. The method is based on longitudinal proton relaxation rate (R_1) measurements at low field (0.01–1 MHz) to assess the localization of ferumoxytol (clinical approved iron oxide particles) in TAM present in melanoma tumours, where $R_1 = 1/T_1$. R_1 at low magnetic fields appears highly dependent on the intra or extra cellular localization of the nanoparticles thus allowing an unambiguous TAM quantification. R_1 profiles were acquired on a Fast Field-Cycling relaxometer equipped with a 40 mm wide bore magnet and an 11 mm solenoid detection coil placed around the anatomical region of interest. The R_1 values measured 3 h and 24 h after the injection were significantly different. At 24 h R_1 exhibited a behavior similar to "in vitro" ferumoxytol-labelled J774A.1 macrophages whereas at 3 h, when the ferumoxytol distribution was extracellular, R_1 exhibited higher values similar to that of free ferumoxytol in solution. This finding clearly indicated the intracellular localization of ferumoxytol at 24 h, as confirmed by histological analysis (Pearls and CD68 assays). This information could be hardly achievable from measurements at a single magnetic field and opens new horizons for cell tracking applications using FFC-MRI.

1. Introduction

The complex relationships between the immune system and the tumour are under intense scrutiny as they are considered an important hallmark of cancer [1]. Tumour-associated macrophages (TAM) are forced by the cancer cells to adopt an anti-inflammatory phenotype and secrete factors to promote angiogenesis and tumour invasion [2]. For these reasons, sensitive, non-invasive, methods capable of quantitative TAM detection are needed for tumour characterization and individual patient stratification to therapies aimed at TAM elimination or polarization to the M1 phenotype with antitumour properties [3–5]. Among imaging modalities, Magnetic Resonance Imaging (MRI) had a key role in the field of oncology over the last few decades. The prominent role of MRI relies on its superb spatial and temporal resolution; its diagnostic power arises basically from the differences in the longitudinal (T_1) and transverse (T_2 and T_2*) proton relaxation times between healthy and pathological tissues. However, routine MRI assessments are often not able to report on the early tissue changes occurring in response to therapeutic treatments [6].

In this context, the use of Ultrasmall Superparamagnetic Iron Oxides NanoParticles (USPIO-NPs) was proposed in many studies because they are taken up by TAM, generating a detectable contrast in T_2-and T_2*-weighted images [7–10]. However the main drawback of this approach is that the observed contrast is unable to discriminate between extra- and intra-cellular USPIO-NPs and it is therefore biased by non-internalized particles. Therefore, there is a need to develop methods sensitive to the localization of NPs. Of course, the applications under consideration not only involves TAM detection but also includes a number of "cell tracking" applications. In fact, there is an open discussion regarding the advantage of imaging protocols to improve the *in vivo* monitoring of cell therapies [11,12].

Recently, ferumoxytol, a USPIO-NP commercialized for the

* Corresponding author.
E-mail address: simonetta.geninatti@unito.it (S. Geninatti Crich).
[1] S·B and M.R.R contributed equally.

https://doi.org/10.1016/j.biomaterials.2020.119805
Received 25 July 2019; Received in revised form 27 December 2019; Accepted 22 January 2020
Available online 27 January 2020

treatment of anemia in adult patients, has attracted interest for clinical imaging applications [13]. Ferumoxytol is a superparamagnetic iron oxide nanoparticle with a hydrodynamic diameter of 30 nm coated with a semi-synthetic low molecular weight carbohydrate shell (precisely, a polyglucose sorbitol-carboxymethylether shell) [14,15]. The core is consistent with a cubic maghemite (γ-Fe_2O_3) crystal structure, irregular in shape and with a mean diameter of approximately 3.25 nm, as shown by the TEM morphological analysis [14].

USPIO particles were extensively used as contrast agents for MRI as they have several advantages over standard small molecular paramagnetic contrast agents including: *i)* higher relaxivity, leading to higher sensitivity; *ii)* specificity to target tumour region delivery via the enhanced permeability and retention (EPR) effect [16]; *iii)* ability to be phagocytosed by cells of the Reticulo Endothelial (RES) and Mononuclear Phagocyte (MPS) systems [17]. Intravenously injected USPIO-NPs distribute in the blood pool and, due to their large size, remain confined to the intravascular space in most organs, except for liver and spleen. In tumours, ferumoxytol slowly extravasates across the highly permeable endothelium of tumour, accumulates in the tumour stroma where it may be phagocytosed by TAM [18–21]. It has been reported that extracellular iron oxides in early tumour necrosis lead to strong T_1 and T_2-enhancement at high (> 3 T) magnetic field while compartmentalized intracellular iron oxides in macrophages are characterized by predominant T_2-with little T_1-enhancement [22,23]. Therefore, these USPIO-NPs were proposed for the quantification of necrotic zones and/or macrophages infiltrating tumour stroma that highly correlate with poor outcome.

Herein, we propose a new alternative diagnostic protocol to assess the localization of ferumoxytol in TAM in melanoma tumours. The method is based on the measurement of proton relaxation rate R_1, where $R_1 = 1/T_1$, as a function of the magnetic field strength (Nuclear Magnetic Resonance Dispersion, NMRD, profile), by using a Fast Field Cycling (FFC) relaxometer. FFC is the only practical way of measuring T_1-dispersion and involves rapid switching of the magnetic field between different field strengths during the measurement procedure. Recently, the prognostic potential of the NMRD profile has been highlighted by our group, using an FFC-relaxometer prototype endowed with a wide-bore magnet and a dedicated transmitter/receiver solenoid detection coil of 11 mm diameter placed around a mouse's leg. Water proton $1/T_1$ NMRD profile measured *in vivo* on implanted mammary tumours showed a marked T_1 elongation at low magnetic fields (< 0.2 T) with respect to healthy tissues [24–26]. Recently, two prototypes human whole-body sized Fast Field Cycling-MRI scanners built at the University of Aberdeen by Lurie's group allowed *in vivo* measurements on human patients thus demonstrating the possibility of translating the preclinical results to clinic. Both instruments can change the magnetic field strengths, between 1 mT and 100 mT in 30 ms for our system and 0.1 mT–200 mT in 15 ms for the Aberdeen FFC-MRI scanner [27]. Pilot studies performed on these FFC-MRI scanners have already demonstrated the potential use of FFC-MRI in a range of several pathologies such us musculoskeletal and cardiovascular diseases [28,29]. Herein we report that ferumoxytol effect on tissue relaxation rates at low magnetic field strengths (0.01–1 MHz as expressed in terms of the corresponding proton Larmor frequencies) is highly dependent on the intracellular or extracellular localization of the magnetic particles thus allowing an unambiguous TAM quantification. Likely, the method can be generalized to other USPIO-NPs, in particular to those characterized by a relatively low R_2/R_1 ratio.

2. Materials and methods

2.1. Cell cultures

B16–F10 (ATCC® CRL-6475™) and J774A.1 (ATCC® TIB-67™) were purchased from American Type Culture Collection (ATCC, USA). They were grown in Dulbecco's modified Eagle's media supplemented with 10% fetal bovine serum (FBS), 100U/mL Penicillin (P) with 100 μg/ml Streptomycin (S). Cells were cultured in 5% CO_2/95% air at 37 °C in a humidified chamber, split every 2–3 days, and used up to passage 10. All cells were tested negative for mycoplasma by MycoAlert™ Mycoplasma Detection Kit. All materials were purchased from Lonza (Basel, Switzerland).

2.2. Ferumoxytol uptake by J774A.1 macrophage and in vitro NMRD profile

For experiments of uptake, 500,000 of J774A.1 were plated in 6 cm dishes 24 h before the incubation with different concentration of Ferumoxytol (Takeda Pharma A/S Roskilde, Danmark) (from 0.06 to 1 mM of Fe). The amount of Fe was measured by ICP-MS procedure, as described below. For NMRD profile experiments, 2 million of J774A.1 were plated and the day after they were incubated in presence of 0.5 and 0.1 mM of Fe for 24 h. The cells were detached with scraper and washed three times with 20 ml of PBS. Then the cell suspension was transferred in the NMR glass tube and the pellet was obtained removing the supernatant after 5 min of centrifugation (0.1 rcf), just before the NMRD profile acquisition. The ^{1}H-NMRD profiles were measured over a range of magnetic field strength from 0.01 to 10 MHz proton Larmor frequency on the Fast-Field Cycling relaxometer (SmartTracer, Stelar S. r.l., Mede (PV)). The typical field sequences used were the Not Polarized (NP) sequence between 10 and 7.5 MHz and the Pre Polarized (PP) sequence between 7.5 and 0.01 MHz. The observation field was set at 7.2 MHz T_1 was determined by the saturation recovery method. Sixteen values of delay (τ) between pulses were used. The number of averaged experiments was two.

2.3. Animal model

6-old-week male C57BL/6 mice were inoculated in muscle hind limb with 750,000 B^{16}–F10 cells in 100 μL of PBS. C57BL/6 (Charles River Laboratories Italia S. r.l., Calco Italia) were maintained under specific pathogen-free conditions in the animal facility of the Molecular Biotechnology Center, University of Turin. All animal experiments have been carried out in accordance with the EU Directive 2010/63/EU for animal experiments. Before imaging and nuclear magnetic resonance experiments, mice were anaesthetized with a mixture of tiletamine/zolazepam (Zoletil 100; Vibac, Milan, Italy) 20 mg/kg and xylazine (Rompun; Bayer, Milan, Italy) 5 mg/kg. The animal treatment protocol was approved by the Italian Ministry of Health (Authorization number 807/2017-PR).

2.4. In vivo NMRD profiles acquisition

^{1}H-NMRD profiles were acquired on a Stelar SPINMASTER FFC NMR relaxometer (Stelar S.r.l., Mede (PV), Italy). Data were acquired with the NP sequence (10 MHz ≤ relaxation field ≤ 7 MHz) or the PP sequence (relaxation field < 7 MHz). The relaxometer operates under complete computer control with an absolute uncertainty in the $1/T_1$ value of ± 2%.

$1/T_1$ NMRD profiles of tumour-bearing mouse (8 points at 0.01, 0.019, 0.037, 0.07, 0.15, 0.387, 1 and 10 MHz) were acquired when the tumour mass was > 65% of the total leg using the relaxometer equipped with a 40 mm 0.5 T FC magnet and a dedicated 11 mm solenoid detection coil. Data were acquired with the above-mentioned sequences with polarization at 13 MHz and detection at 14.5 MHz, a field switching time of 4 ms, a 90° pulse length of 5.5 μs. Thirty-two incremented relaxation delay were logarithmic distributed from 0.01 to 2.8 s for the points in the field range 0.01–0.07 MHz and from 0.01 to 4 s for the points in the field range 0.15–10 MHz.

The NMRD profiles were carried out before (PRE), 3 and 24 h after (POST) the ferumoxytol injection (0.5 mmol/kg dose of Fe).

The magnetization recovery data were analysed according to a

mono-exponential decay (Bloch equation) and the two-Site eXchange model (2SX model, see below) with Origin software (OriginPro 8.5.0 SR1, OriginLab, Northampton, MA, Levenberg-Marquardt algorithm).

2.5. Immunochemistry assay

Immediately after the NMRD profile, the mice were sacrificed and perfused via the vascular system with 4% paraformaldehyde (PFA), as fixation procedure, in order to obtain the best possible preservation of the tumour tissue for immunohistochemistry [30].

PFA-fixed and paraffin-embedded tissue sections were stained with haematoxylin & eosin. For immunohistochemistry assays, de-waxed 5 μm sections were submitted to wet heat-induced antigen retrieval in a mixture of 0.1 M Tris and 0.01 M EDTA solution at pH 9.0. Endogenous peroxidase was blocked in 0.6% hydrogen peroxide solution in 0.05 M TBS (pH 7.6) for 20 min at room temperature. Sections were then treated with 5% normal goat serum and reacted overnight with rabbit anti-mouse CD68 (ab125212; Abcam). Subsequently, sections were incubated with goat anti-rabbit (ab97051; Abcam) IgG conjugated to HRP for 1 h at room temperature. Finally, sections were treated with diaminobenzidine-enhanced liquid substrate chromogen system (D3939; Sigma-Aldrich) and counterstained with haematoxylin.

For Perls staining, tissue sections were de-waxed and treated with a solution of 5% potassium ferrocyanide and 5% hydrochloric acid for 1 h at room temperature. Finally, sections were counterstained with Nuclear Fast Red solution (Sigma).

For CD68 and Perls staining on the same tissue section, CD68 IHC was performed as stated above. After incubation with secondary antibody conjugated to HRP, sections were treated with AEC substrate (Abcam) and mounted with glycerol. Several images were acquired with optical microscope (Olympus BX41). Then cover glasses were removed and slides were rinsed in alcohol 99% and xylene in order to dissolve AEC substrate. Finally, the same slides were used for Perls staining, counterstained with Nuclear Fast Red solution and mounted in synthetic mounting. Perls images of the same section were acquired as above. Images of the same region were overlapped with ImageJ software in order to obtain a merge of the two staining techinques (CD68 and Perls).

2.6. Inductively coupled plasma mass spectrometry (ICP-MS)

Fe content from cell samples and ferymoxytol solutions were determined using inductively coupled plasma mass spectrometry (ICP-MS) (Element-2; Thermo-Finnigan, Rodano (MI), Italy). Sample digestion was performed by means of microwave heating for 10 min at 160 °C in 1 mL of concentrated HNO_3 (70%) (Milestone, Ethos Up Microwave Digestion System, Bergamo, Italy). A natural abundance iron standard solution was analysed during sample runs in order to check for variations in the systematic bias. The calibration curve was obtained using four iron absorption standard solutions (Sigma-Aldrich) in the range 0.2–0.005 μg/mL.

2.7. The two-site eXchange (2SX) model

In the two-Site eXchange (2SX) model, the Bloch equations for nuclear magnetic resonance were modified to describe two compartments (intra and extracellular) in which water exchange modulates the observed relaxation behavior [31–34]. The time evolution of M_Z depends on the absolute values of the relative size of the "relaxation" term, $|R_{1in} - R_{1ex}|$, and of the "exchange" term $k_{in} + k_{ex}$, (where $k_{in} = 1/\tau_{in}$ is the water exchange rate from the extracellular to the intracellular compartment and $k_{ex} = 1/\tau_{ex}$ is the water exchange rate in the opposite direction). This relationship was previously defined as the NMR "shutter-speed".

The PRE data were simultaneously analysed, sharing the V_{ex} and τ_{in} parameters but maintaining R_{1ex} fixed to the value obtained from Matrigel in a separated experiment, in order to reduce the number of parameters to fit [24]. The parameter V_{ex} was allowed to vary within a reasonable range, in accordance with results already reported in the literature (0.15–0.5) for tumour mouse hind-limb [35–37].

In the case of the NMRD profiles acquired 24 h after the ferumoxytol injection, the R_{1in} term is expressed as follows:

$$R_{1in} = R_{1in}^0 + [Fe]\cdot r_1 \quad (1)$$

where $R_{1in}{}^0$ is the contribution in the absence of ferumoxytol, [Fe] and r_1 are the ferumoxytol intracellular concentration (calculated from the contrasted images acquired at 7 T, as described above) and relaxivity, respectively. The $R_{1in}{}^0$, V_{ex} and τ_{in} values were fixed at the values found in the analysis of the corresponding PRE-contrast NMRD profiles.

2.8. Magnetic Resonance Imaging (MRI)

MR images of the mouse limb region were acquired on a 7 T Bruker AV300 spectrometer equipped with a Micro 2.5 microimaging probe and a birdcage resonator with 30-mm inner diameter. Images were recorded the same day as the acquisition of the NMRD profiles before and after the injection of ferumoxytol (0.5 mmol/kg of Fe). The distribution of ferumoxytol in the tumour region was followed by measuring T_1 by means of a saturation recovery sequence (TE = 3.3 ms; number of slices = 3; slice thickness = 2 mm; FOV 30 × 30 mm; matrix 32 × 32), before, 3 h and 24 h after injection of the contrast agent. The tumour volume was measured from T_2-weighted MRI images obtained by using a rapid acquisition with refocused echoes sequence protocol (TR = 5000 ms; TE = 28 ms; number of slices = 11; slice thickness = 1 mm; FOV 50 × 50 mm; matrix 168 × 160).

Assuming the occurrence of a fast-exchange regime (i.e., $|R_{1in} - R_{1ex}| \ll k_{in} + k_{ex}$) [38] at 7 T, the effective intratumour Fe concentration, $[Fe]_{eff}$, was determined by Equation (2)

$$[Fe]_{eff} = (R_1^{POST} - R_1^{PRE})/r_{1i} = \Delta R_1/r_{1i} \text{ with } i = \text{in or ex} \quad (2)$$

where $R_1{}^{POST}$ and $R_1{}^{PRE}$ are the relaxation rates measured after and before ferumoxytol injection; r_{1ex} is the millimolar relaxivity of ferumoxytol, measured at 7 T, in Matrigel (used as extracellular matrix model, $r_{1ex} = 2.4\ mM^{-1}\ s^{-1}$); r_{1in} is the millimolar relaxivity of ferumoxytol, measured at 7 T, on J774A.1 cells incubated for 6 h with ferumoxytol dissolved in the culture medium at a 0.02 mM Fe concentration ($r_{1in} = 1.05\ mM^{-1}\ s^{-1}$). After incubation cells were washed three times with cold PBS, detached with scraper, transferred into the 5 mm NMR tube and centrifuged 5 min at 0.1 rcf. Fe concentration remaining into the cell pellet was determined by ICP-MS.

The $[Fe]_{eff}$ is the effective value of the tissue concentration, as it refers to the sum of the intracellular and extracellular volumes. Then, the Fe concentration in the extracellular and intracellular volume fraction (V_i) is given by Equation (3)

$$[Fe]_i = [Fe]_{eff}/V_i \text{ with } i = \text{in or ex} \quad (3)$$

2.9. Calculation of the fraction of macrophages in the tumour tissue

The equation for the calculation of macrophage fraction was derived as following:

$$\%\ \text{TAM in tumour tissue} = \frac{number\ of\ TAM}{total\ cell\ number\ in\ the\ tissue} \times 100 \quad (4)$$

where the total number of cells in 1 g of tissue was considered to be 10^9 [39]. The number of TAM in 1 g of tissue was expressed as

$$\text{Number of TAM in 1 g of tissue} = \frac{mmol\ of\ Fe\ in\ 1\ g}{mmol\ of\ Fe\ per\ TAM\ cell} \quad (5)$$

where the quantity of iron in mmol in 1 g is:

$$\text{mmol of Fe in 1 g} = \frac{[R_1^{24h\ POST} - R_1^{PRE}] + 0.41}{7} \times 0.001 = \frac{\Delta R_1^{24\,h} + 0.41}{7} \times 0.001 \quad (6)$$

where the mmol of Fe per TAM cell was calculated using J774A.1 incubated 24 h in the presence of ferumoxytol 0.005 mM. After cell washing and detaching Fe was determined by ICP-MS and normalized to the cell number. The 0.005 mM ferumoxytol concentration was used because the corresponding r_1 at 1 MHz (7 mM^{-1} s^{-1}) equal to that found in tumour tissue *in vivo*.

Equation 7 is obtained by combination of equations (4)–(6):

$$\%\ \text{TAM in tumour tissue} = \frac{(\Delta R_1^{24\,h} + 0.41)}{mmols\ of\ Fe\ per\ cell \times 7} \times 10^{-10} \quad (7)$$

2.10. Isolation of mouse tumour-associated macrophages (TAM)

After the acquisition of $1/T_1$ NMRD profile at 24 h post ferumoxytol injection, the protocol for the isolation of TAM from tumour tissue was applied. Next the gently separation of the tumour from the healthy muscle, the tumour weight was measured and blended tumour tissue was suspended in free Serum medium (0.2 mg/2 ml) adding 20 μl of collagenase (0.1 mg/ml) mixed at 37 °C for 45 min applying continuous rotation. The tumour lysate was filtered with 70 μm cell strainer in a 50 ml tube and centrifuged 5 min at 0.4 rcf adding 20 ml of PBS. The red blood cell lysis buffer was added at supernatant for 20 min at RT and then the solution was centrifuged 5 min at 0.4 rcf adding 20 ml of PBS. The pellet was suspended to 1×10^6 cells/ml and 1 ml was transferred to a 5 ml polystyrene tube. After the Fc blocking (Miltenyi Biotec GmbH) for 5 min at RT, single cell suspensions were obtained and stained with anti-CD45-VioGreen, anti-F4/80-PE/Vio770 and anti-CD11b-FITC. Samples were analysed on a BD FACSVerse and analysed using BD FACSSuite software.

3. Results and discussion

The dynamics of ferumoxytol particles did not appear to change significantly between suspensions in water and in a model of extracellular media. Fig. 1 shows the $1/T_1$ NMRD profile of a ferumoxytol suspension in water (37 °C) and in matrigel (37 °C and 30 °C). Matrigel is the trade name for a gelatinous protein mixture secreted by Engelbreth-Holm-Swarm (EHS) mouse sarcoma cells. It is considered a good model of the extracellular matrix and is used as a substrate for cell cultures [24,40].

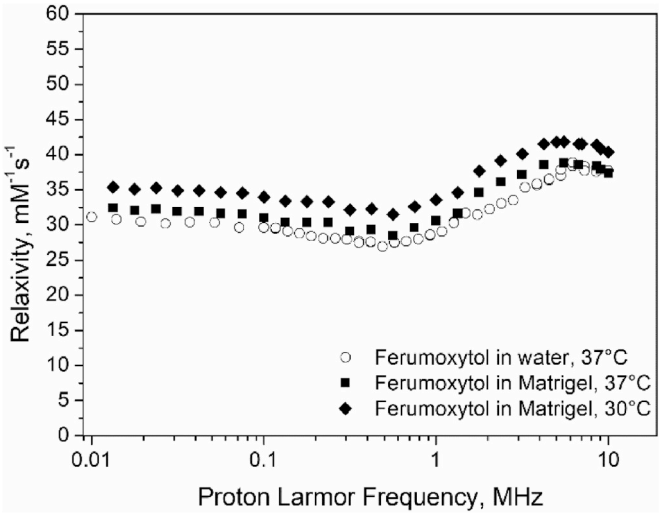

Fig. 1. $1/T_1$ NMRD profile of a ferumoxytol solution in water (37 °C) and in matrigel (37 °C and 30 °C).

Interestingly, the iron relaxivity (the relaxation rate per unit concentration, r_1 in mM^{-1} s^{-1}) in both water and matrigel is greater than 25 s^{-1} mM^{-1} over the entire range of magnetic fields observed. Several theories are available to describe relaxation for small and large iron oxide particles [41–43] and they can provide some insights on the dynamics of the system.

As described by Roch's heuristic model [44], at high field the relaxation rate only depends on τ_D (translational correlation time) and the inflection frequency f_I corresponds to the condition defined by $\omega_I\tau_D \sim 1$, where $\omega_I = 2\pi f_I$. Since $\tau_D = r^2/D$, where D is the water diffusion coefficient (2.3×10^{-5} cm^2 s^{-1} at 25 °C), and r is the radius of the particles, the determination of τ_D from the NMRD profile allows one to estimate the distance of minimum approach for the water molecules diffusing at the surface of the particles. This informs on water mobility in the vicinity of the particle. At very low fields the relaxation rate is directly proportional to the size of the magnetic core and to the energy of the crystal anisotropy. The Néel relaxation time τ_N depends on the latter and relates to the relaxation of the global magnetic moment of the particle. Hence the relatively high anisotropy of ferumoxytol magnetic core provides it with a relatively high relaxivity even at low magnetic field strengths.

Fig. 1 shows the close similarity between the $1/T_1$ profiles acquired in water and in matrigel thus supporting the view that water mobility (and thus diffusion coefficient) is maintained in both systems despite the higher viscosity of the latter [25].

3.1. NMRD profiles of murine macrophages (J774) in vitro labelled with ferumoxytol

Before carrying out *in vivo* studies, we evaluated the changes in the relaxivity of ferumoxytol due to intracellular and intra-organelles compartmentalization (endosomes, lysosomes). To do this we acquired the NMRD profiles of J774A.1 cell line incubated with ferumoxytol. J774A.1 are a murine monocyte-derived macrophage cell line, often used as phagocytic cell models simulating particle uptake occurring in tumour stroma by TAM [45]. In the case of cellular internalization of Gd-based complexes, it has been already reported [46–49] that, upon increasing the concentration of Gd-complexes in the endosomal compartments, a “quenching” effect on the observed relaxivity takes place. In fact, when the intravesicle concentration of the imaging probe is high (thus resulting in a very large intravesicle relaxation rate), the exchange regime between vesicles and cytosol becomes slow with respect to the differences in relaxivities of the two compartments. Therefore, the relaxation rate of the cytosol compartment is only slightly enhanced by the presence of the entrapped magnetic species. In other words, the water exchange across the vesicle membrane sensibly limits the relaxation rate of the cytosolic water protons compared with the same amount of probe dissolved in the cytosol.

J774A.1 cells were incubated for 24 h at 37 °C with different concentrations of ferumoxytol. For the NMRD profile acquisition, 20 million cells were transferred in 5 mm NMR tubes and centrifuged with 1 ml of PBS (phosphate saline buffer) at 0.1 rcf for 5 min. As shown in Fig. 2, the NMRD profiles of ferumoxytol-labelled J774A.1 cells are very different from those obtained from a ferumoxytol aqueous solution. In particular, the relaxivity peak at ca. 8–10 MHz in water is shifted to lower magnetic field strengths (0.8–1 MHz) as a consequence of the modification of the diffusion coefficient (D). The model used here predicts that D can influence both the amplitude and the position of the R_1 peak due to the local increase of water viscosity in the immediate vicinity of the magnetic nanoparticles, which causes an increase in τ_D. Note that increasing the particle size is equivalent to decreasing the diffusion coefficient D and would shift the relaxivity peak further down along the frequency axis.

Most importantly, the values taken by the relaxivity profiles for ferumoxytol-bearing cells are significantly lower than those ones

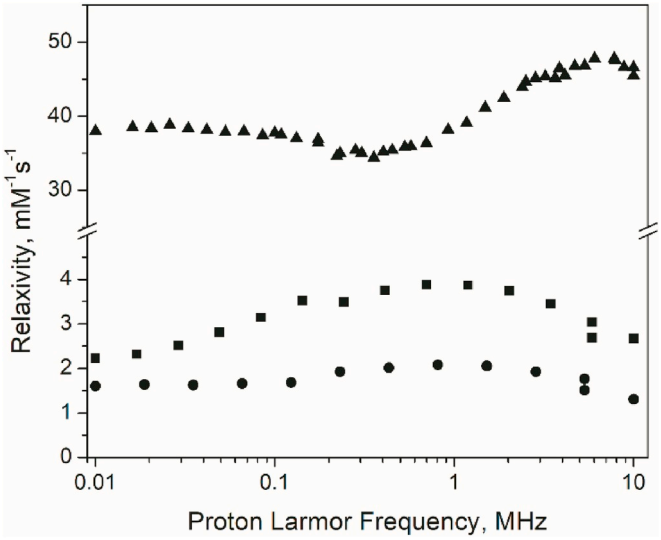

Fig. 2. NMRD profiles, acquired at 25 °C, of J774A.1 cells labelled with ferumoxytol with two different Fe concentration 2.2 (■) and 14.5 (●) mM, respectively. Filled triangles (▲) correspond to the NMRD profile of ferumoxytol alone dissolved in buffer. The indicated concentrations refer to the Fe concentration in the cell pellets measured by ICP-MS. The relaxation rates are normalized to the residual Fe concentration found in cell pellets measured by ICP-MS.

observed for ferumoxytol in neat buffer solution at any magnetic field. This is due to the occurrence of a relaxivity "quenching" upon ferumoxytol compartmentalization in intracellular vesicles (endosomes, lysosomes) in analogy to what has already been observed with Gd-complexes [46–49]. When nanoparticles are incubated in a cell suspension, the endo-phagocytic uptake ends up placing them into vesicles arising from the invagination of the cytosolic membrane [50]. This locally increases the concentration of particles, which lowers their overall relaxivity as explained above. Fig. 2 shows that the "quenching" effect on r_1 is inversely proportional to the Fe concentration taken-up by cells. In fact, an increase of intravesicular Fe concentration corresponds to a more pronounced relaxivity "quenching" effect. From these results, one may conclude that the contribution to the overall ^{1}H relaxation rate generated by intracellular ferumoxytol is markedly smaller than the value measured when the same amount of magnetic particles are suspended in the extracellular medium. Moreover, the acquisition of R_1 values at different frequencies allows us to extract useful information on the localization of magnetic particles that is not available from measurements carried out at fixed and high magnetic fields. This finding appears extremely important for monitoring the fate of labelled cells *in vivo*.

3.2. Ferumoxytol in melanoma (B16–F10) grafted tumour models

The possibility to characterize ferumoxytol internalization was then tested *in vivo*. B16–F10 melanoma cells were implanted in mice leg (n = 12) following the protocol described in material and methods. The position of the graft was dictated by the round shape of the detection coil and its diameter (11 mm) [24]. It is well known that neoformed vessels of solid tumour show a significantly higher permeability to nanoparticles that leads to larger accumulation compared with healthy tissues (EPR effect), hence this model was expected to show large USPIO contrast. Due to the lack of spatial resolution, NMRD profiles on living tumour tissues were acquired only when the tumour mass was > 65% of the total leg tissue in order to minimize partial volume effects. Under this condition, healthy muscle only affects the observed relaxation rates to a limited extent (Fig. 3A). The selected types of tumours B16–F10 murine melanoma are characterized by a high amount

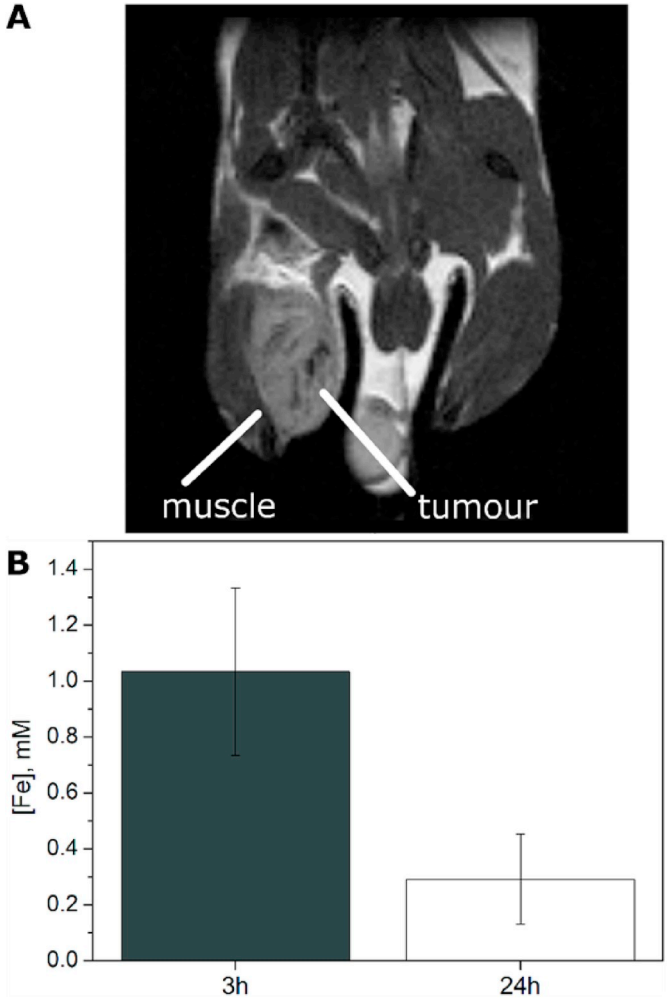

Fig. 3. (A) T_2-weighted MRI (7 T) of the tumour-bearing mouse (B16–F10 graft). (B) Fe concentration in the B16 tumour tissue at 3 h (mostly extracellular, n = 7) and 24 h (mostly intracellular, n = 11) after ferumoxytol i. v. administration. Concentrations were calculated starting from T_1 data, acquired at 7 T. Error bars represent the Standard Deviation.

of macrophages infiltrating the tumour stroma [51–53]. Therefore the amount of ferumoxytol remaining in the tumour 24 h after the injection was expected to be high due to an efficient uptake by TAM. Ferumoxytol was injected at the dose of 0.5 mmol Fe/kg and the accumulation in tumour tissues was assessed 3 and 24 h after by measuring T_1 at 7 T (Fig. 3B), followed directly by the acquisition of the NMRD profile in order to deal with strictly analogue anatomical and functional conditions. A period of 3 h post contrast appeared a good compromise to maximize the extravasation of the nanoparticles into tumour meanwhile to minimize the macrophages phagocytosis, which is expected to increase markedly after 24 h. During this time, the clearance of not internalized nanoparticles takes place [6,7,23,54,55]. The use of a high magnetic field strength ensured the observation of a fast exchange regime to satisfy the condition $|R_{1in} - R_{1ex}| \ll k_{in} + k_{ex}$, where R_{1in} and R_{1ex} are the intra- and extra-cellular relaxation rates respectively and k_{in} and k_{ex} are the water efflux and influx rates, respectively. This ensures that the magnetization recovery remained monoexponential and that the measurement of the relaxation rate was independent of the presence of intra and extracellular compartments [24,25,38].

As expected the amount of ferumoxytol measured 24 h after the injection was significantly lower than that measured at 3 h. In fact, after 24 h most of the ferumoxytol was washed out by the tumour stroma and the remaining particles were mostly internalized into macrophages.

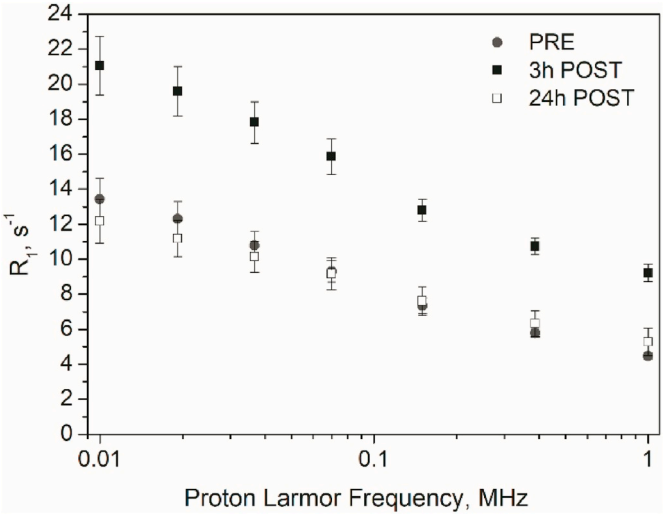

Fig. 4. NMRD profiles of tumour-bearing mouse legs before (PRE), 3 and 24 h after (POST) the i. v. injection of ferumoxytol.

Fig. 4 shows the R_1 values obtained by the monoexponential fitting of magnetization recovery from 0.01 to 1 MHz of B16–F10 tumour mouse model at 3 h (n = 6) and 24 h (n = 12) after administration of nanoparticles.

As expected, a marked relaxation enhancement was observed 3 h after injection of ferumoxytol at any magnetic field strength. This enhancement was quite pronounced both at 1 (+106%) and 0.01 MHz (+57%). After 24 h the almost complete ferumoxytol wash-out from the tumour yielded a dramatic decrease of the relaxation enhancement. In order to isolate the ferumoxytol contribution from the overall relaxation rates, the pre-treatment R_1 was subtracted to the profiles acquired 3 and 24 h post-ferumoxytol administration (Fig. 5A). For convenience we will indicate as $\Delta R_1^{3\ h}$ and $\Delta R_1^{24\ h}$ the dispersion profile data resulting from the measurement acquired at 3 h and 24 h post injection upon subtraction of the pre-injection data.

$\Delta R_1^{24\ h}$ exhibited an overall shape that appeared very different from $\Delta R_1^{3\ h}$: its profile invariantly displayed a positive slope (calculated in the range 0.01–0.07 MHz) with a maximum around 0.8–1 MHz (Fig. 6A) similar to the one found for ferumoxytol-labelled J774A.1 macrophages, whereas $\Delta R_1^{3\ h}$ yielded negative slopes (calculated in the range 0.01–0.15 MHz). Thus, the R_1 slopes obtained at 3 and 24 h after ferumoxytol treatment (Fig. 5B) appear as the most significant parameter to use since they are unequivocal reporters of the localization of ferumoxytol nanoparticles. The positive slope observed at 24 h is similar to that observed for J774A.1 incubated with ferumoxytol (Fig. 6) thus supporting the view that, *in vivo* and after 24 h, the relaxation enhancement observed arises essentially from the cellular-entrapped ferumoxytol. On the contrary, the R_1 profile acquired immediately after dissolving ferumoxytol nanoparticles into the extracellular space of J774A.1 without incubation at 37 °C (Fig. 6) shows the same behavior as observed *in vivo* 3 h after ferumoxytol administration, once subtracted from the profile of untreated cells. Note that the profiles showed in Fig. 5A are in the range 0.01–1 MHz because the R_1 value measured at 10 MHz deviates from the expected trend. This could be the consequence of the dramatic decrease of T_2* induced by iron oxide particles occurring between 1 and 10 MHz [44] that may cause an error in T_1 estimation [56].

Moreover, by plotting $\Delta R_1^{24\ h}$ measured at the maximum of the relaxation peak (1 MHz, Fig. 5A) as a function of the effective intratumour Fe concentration as determined at 7 T, one can obtain an average relaxivity r_1 at this field (r_1 = 7 $mM^{-1}\ s^{-1}$) that can be used to determine the intracellular Fe concentration in unknown samples (Fig. 7).

Thus, supposing a linear behavior for $\Delta R_1^{24\ h}$ as shown in Fig. 8, a

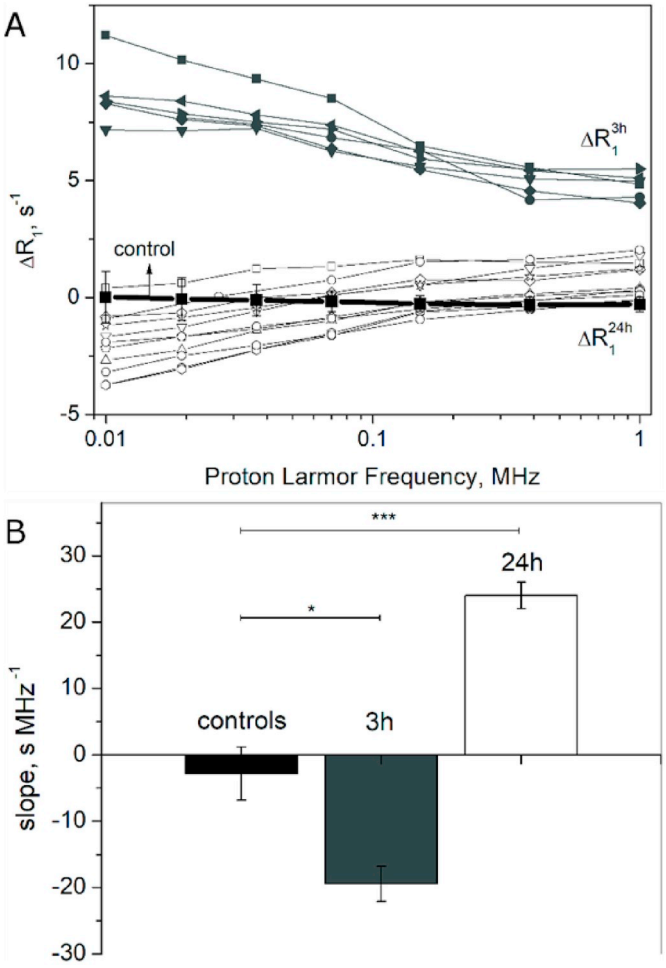

Fig. 5. A) ΔR_1 curves, obtained by subtracting pre-treatment profiles to the corresponding post-treatment profiles acquired 3 h (dark gray filled symbols, n = 6) and 24 h (open symbols, n = 11) after ferumoxytol administration to mice bearing melanoma tumours. Black squares correspond to the control for POST and PRE profiles acquired 24 h after the injection of a physiological solution; B) Average Slopes of ΔR_1 profiles. Statistical significance was determined by Student's t-test: P = 0.0133 (3 h); P = 0.00003 (24 h) (***P < 0.01, *P < 0.05).

semi-quantitative estimation of the fraction of macrophages present in the tumour 24 h after ferumoxytol injection can be obtained using the following equation (derived as described in materials and methods):

$$\%\ \text{TAM in tumour tissue} = \frac{(\Delta R_1^{24\,h} + 0.41)}{\text{mmols of Fe per cell} \times 7} \times 10^{-10} \quad (7)$$

where $\Delta R_1^{24\ h}$ is the difference in tissue relaxivities as defined above, when measured at 1 MHz. The amount of Fe per cell (1.5×10^{-12} mmol of Fe/cell) was measured by Inductively Coupled Mass Spectrometry (ICP-MS) in J774A.1 cells incubated for 24 h with ferumoxytol 0.005 mM (Fe concentration). The use of this ferumoxytol concentration yielded a r_1 relaxivity equal to that determined *in vivo* at the same magnetic field (1 MHz). Using this equation it was possible to obtain the fraction of macrophages inside the tumour tissues, ranging from 2.7% to 21% in the melanoma-bearing animals considered in this study. These percentages are in good agreement with those ones found in the literature for melanoma tumours [57]. Moreover, the estimated TAM % were compared with those obtained by flow cytometry after collagenase digestion on the same tumour tissues [58]. (Table 1) The agreement of the two methods was assessed by the Bland and Altman statistical method [59,60] with a confidence level of 95% (see Fig. S2, supplementary materials).

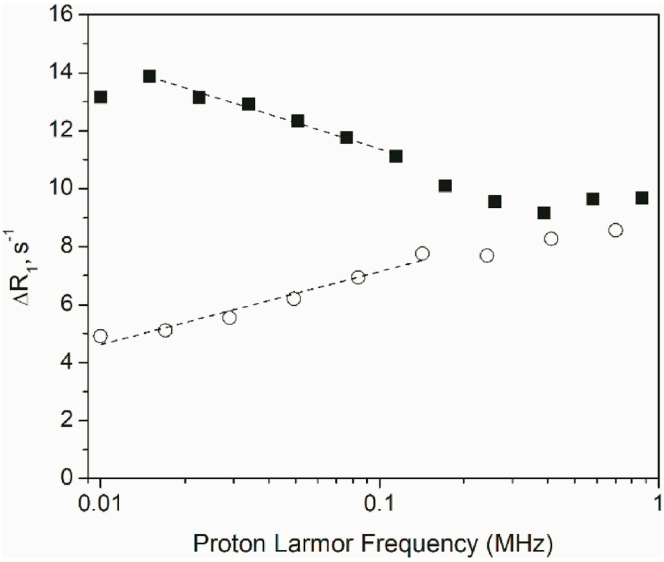

Fig. 6. R_1-difference curves, obtained on J774A.1 cells incubated in vitro with ferumoxytol (0.1 mM) for 24 h (open circles) or J774A.1 cells simply exposed to ferumoxytol (1 mM) in the external PBS solution without incubation at 37 °C (black filled squares).

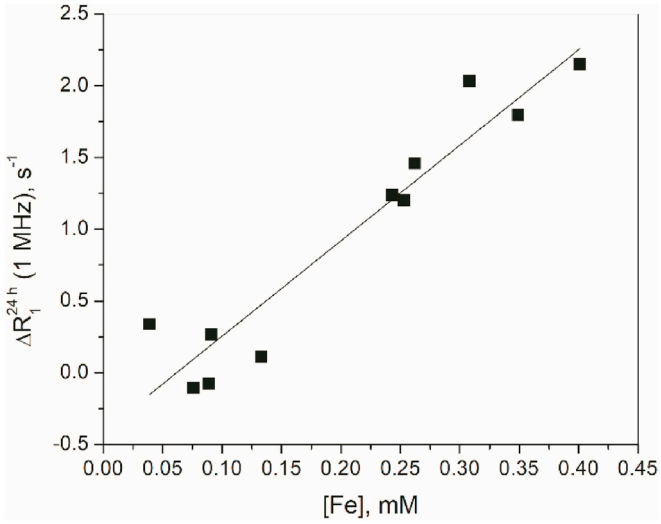

Fig. 7. $\Delta R_1^{24\ h}$ measured at 1 MHz as a function of the effective intratumour [Fe] mM measured at 7 T.

3.3. Assessment of ferumoxytol localization in tumour tissue

The results described above needed to be validated by microscopy to verify that ferumoxytol was indeed internalized by macrophages 24 h after exposure. Immediately after the NMRD profile acquisition, mice were sacrificed to carry out histological analysis using the Perls' (Prussian Blue) stain protocol to assess intratumoural localization of contrast agent. In Fig. 8, the Perls staining positivity of histological sections is shown at 3 and 24 h after the injection of ferumoxytol, compared to control sections. At 3 h after the administration, the distribution of the Perls stain was largely diffuse with an extracellular localization, especially in the haemorrhagic area and on the border between muscle and tumour, indicated with the letter M and T in the figures, respectively. At 24 h, in the same area, the Perls staining appeared to have a largely dominant intracellular location, more appreciable at high magnification. In particular, in Fig. 8F the Perls stain positivity is clearly detectable in cytoplasmic area surrounding the nucleus, as the black arrows indicate.

Fig. 9 shows that the tissue slice distribution of CD68 staining positivity was comparable with Perls staining accordingly to the iron nanoparticle localization inside macrophages.

In order to unequivocally demonstrate that the ferumoxytol remaining in the tumour tissue 24 h after its injection is taken up only by TAM, it was necessary to carry out CD68 and Pearls staining on the same tissue slide. To avoid any interference between Perls staining, which involves the use of 5% hydrochloric acid solution, and CD68 immuno-detection, a dual-step staining procedure was performed. First immunohistochemistry for CD68 was carried out and several images were acquired with optical microscope. Then AEC substrate was completely removed by dipping the slide in alcohol and xylene. Finally, Perls staining was performed on the same slide and images of the same field were acquired. Fig. 10 shows that only macrophages (positive to CD68 staining) exhibit positivity to Perls staining whereas the remaining tumour cells are negative to both staining. The absence of ferumoxytol internalization by tumour cells was reported also in the studies published by Daldrup-Link H. E. (2012) [61] and Cao Q. (2018) [62] performed in different types of tumours.

3.4. Intracellular ferumoxytol relaxivity ($mM^{-1}\ s^{-1}$) estimated by the 2 site eXchange model (2SX)

So far we analysed the magnetization decay using a mono-exponential model. This may draw some criticisms since the system studied is a multi-compartmental one. Herein, a more in-depth approach is carried out with the aim of assessing the intracellular ferumoxytol relaxivity. As the vascular space occupies a small tissue fraction, both healthy and tumour tissues can be approximatively described as systems composed of two compartments, one intracellular and another extracellular. During the time required by a NMR relaxation measurements or an image acquisition, water can explore both compartments and the resulting R_1 results from a mixing of their relaxation rates R_{1in} and R_{1ex} weighted by their respective volume fractions (V_{in} and V_{ex}). This two-compartments situation is described by the 2SX model, which we will use here to extract quantitative parameters from the system [31–34]. (Fig. 11).

In the absence of paramagnetic labelling, differences in the relaxation rates of the two compartments are inversely proportional to the magnetic field strength, since R_{1ex} has a much less pronounced magnetic field dependence with respect to R_{1in} [24,31]. When, at certain magnetic fields, these differences reach the same order of magnitude as the exchange rate across the cellular membranes (i.e. $|R_{1in}-R_{1ex}| \sim k_{in} + k_{ex}$) a biexponential magnetization decay becomes evident. The occurrence of this condition allows extracting two apparent contributions, one characterized by the longer and one by the shorter longitudinal relaxation time. Under these conditions the decay of the longitudinal magnetization M_z depends not only from the values of R_{1in} and R_{1ex} but also on how fast water exchange takes place between the two compartments. It was shown that, at the high magnetic field strength of clinical scanners, the fulfillment of these conditions may be reached by adding high concentrations of paramagnetic Gd complexes to the extracellular compartment [46–49]. Therefore, τ_{in} (intracellular water residence time, $1/k_{in}$) and τ_{ex} (extracellular water residence time, $1/k_{ex}$) are introduced in the 2SX fitting model of the magnetization recovery curves [31–34]. Such residence lifetimes are correlated, accordingly to the mass balance, through the volume fraction values of the two compartments:

$$\tau_{in} \times V_{ex} = \tau_{ex} \times V_{in} \quad (8)$$

To get an estimation of the different parameters, M_Z recovery was acquired over an extended number of relaxation delays (n = 32) to improve the sampling of both fast and slow T_1 components while applying the Saturation Recovery procedure. We have recently shown by the *in vivo* acquisition of $1/T_1$ NMRD profiles of mammary adenocarcinoma (on the same prototype FFC-NMR spectrometer used in this

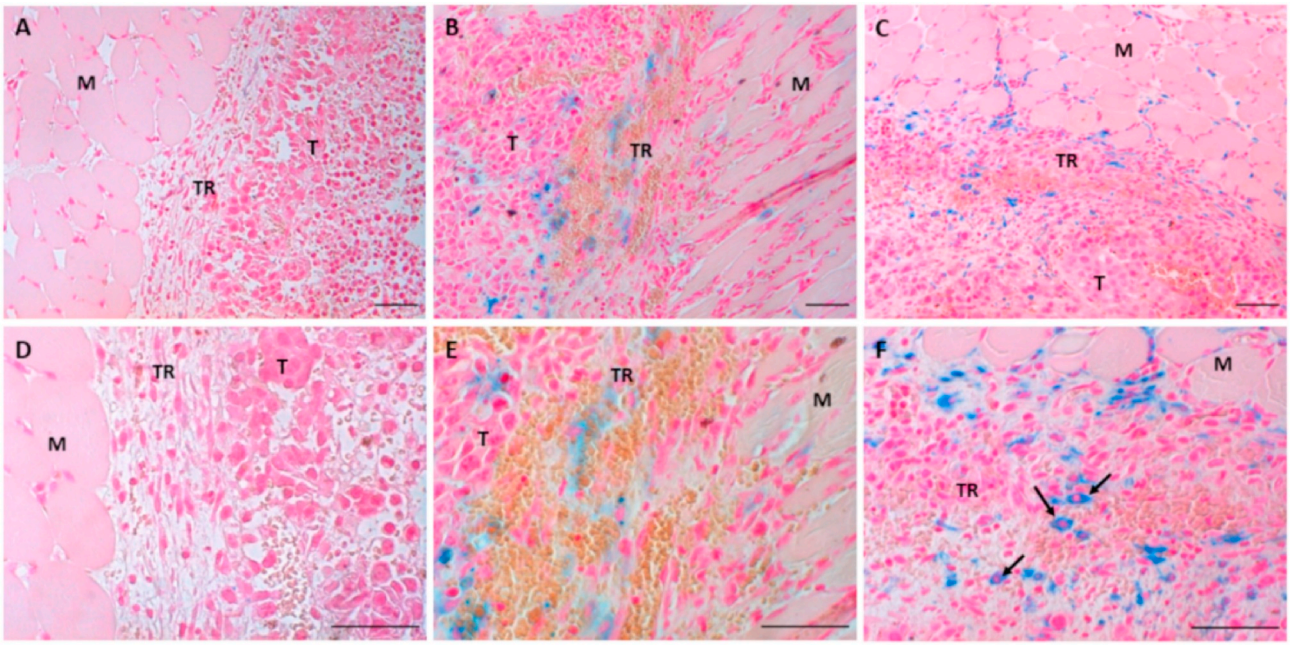

Fig. 8. Perls staining of a representative melanoma B16–F10 tumour tissue. (A-C magnification 20×; D-F magnification 40x). A, D: Nuclear Fast Red (NFR) staining of an untreated control tumour, B, E: NFR and Perls staining 3 h after ferumoxytol injection, C, F: NFR and Perls staining 24 h after ferumoxytol injection. M indicates muscle tissue, T indicates tumour tissue, the arrows indicates iron deposits inside macrophages. Scale bars, 50 μm. (For interpretation of the references to colour in this figure legend, the reader is referred to the Web version of this article.)

Table 1
Comparison of TAM determination by flow cytometry (FACS) and relaxometry (NMRD).

TAM% by FACS	TAM % by NMRD
5	12
10	10
9	5
10	5
11	19
7	19
6	7
14	23

study) that water exchange rates across the cellular membrane can be assessed by measuring water T_1 over an extended range of magnetic fields. This result has been achieved, in the absence of paramagnetic species, thanks to the more pronounced relaxation differences between two compartments observed at low field [24]. On this basis, the NMRD profiles of the mouse melanoma tumours acquired just before ferumoxytol injection (Fig. 4) were analysed according to the 2SX model, while fixing the extracellular R_{1ex} to the values obtained at the same field with matrigel alone. The parameters obtained from the fitting are: $\tau_{in} = 1.31 \pm 0.32$ s, $V_{ex} = 0.26 \pm 0.03$. The averaged R_{1in} values obtained at the different magnetic fields are reported in the supplementary materials (Supplementary Information, Fig. S1).

The administration of ferumoxytol was expected to affect the intra- and extra-cellular compartments to a different extent depending on its distribution. In fact, 3 h after the injection, ferumoxytol was mostly distributed in the extracellular matrix of the tumour and therefore it was expected to significantly increase R_{1ex}. Conversely, 24 h after, the remaining contrast agent was localized intracellularly (as demonstrated by the Perls' Prussian blue staining) and therefore it contributed to further enhance the R_{1in} term. The high relaxivity of ferumoxytol ($r_1 > 30$ $mM^{-1}s^{-1}$ in matrigel) at any applied magnetic field (0.01–1 MHz) and its relatively high concentration in the extracellular space reduced the differences of relaxivities between the two compartments so that $|R_{1in}\text{-}R_{1ex}| < k_{in} + k_{ex}$. Under this condition, the M_z decays observed were almost completely monoexponential and did not depend on the water exchange rate between the two compartments. Moreover, it was difficult to assume which one was the fast or slow site to be considered in the 2SX model. On the other hand, the intracellular localization of ferumoxytol observed 24 h post i. v. simplified the model

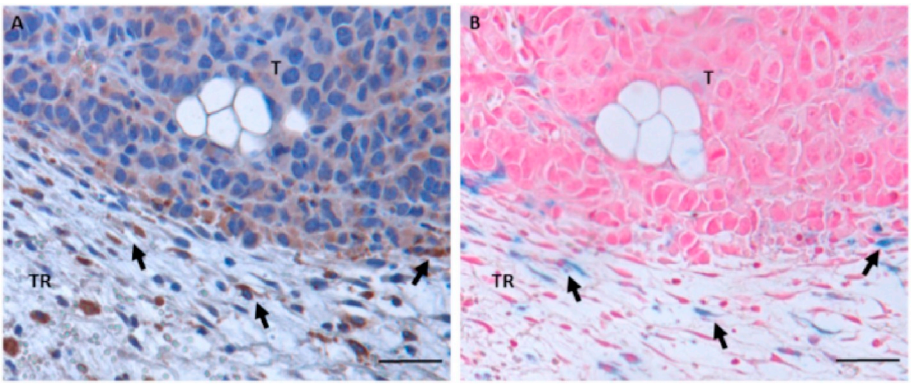

Fig. 9. Comparison between (A) CD68 (cell nuclei counterstained with haematoxylin) and (B) Pearls (cell nuclei counterstained with nuclear Fast Red) staining on two adjacent slices (5 μm) (magnification 40x). T and TR indicate tumour tissue and tumour rim, respectively. Arrows indicate macrophages. Scale bars, 25 μm. (For interpretation of the references to colour in this figure legend, the reader is referred to the Web version of this article.)

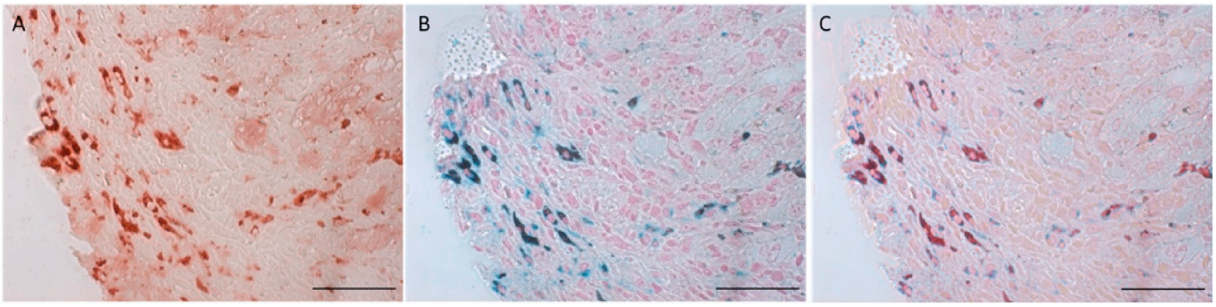

Fig. 10. Perls and CD68 staining of a representative melanoma B16–F10 tumour tissue 24 h after the injection of ferumoxytol. A, IHC for CD68 antigen. B, Perls staining showing intracellular iron/ferumoxytol localization, counterstained with Nuclear Fast Red. C, merge of CD68 and Perls staining performed on the same tissue slide. Scale bars, 50 μm. (For interpretation of the references to colour in this figure legend, the reader is referred to the Web version of this article.)

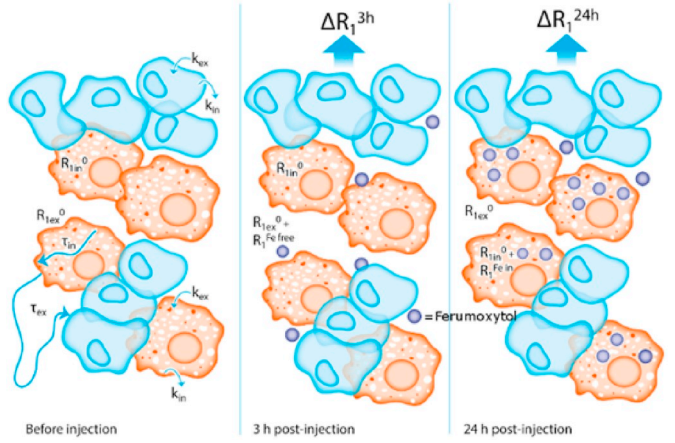

Fig. 11. A schematic representation of melanoma tumour tissue before, 3 and 24 h after the ferumoxytol injection. Blue and brown cells correspond to melanoma and TAM, respectively. The parameters k_{in}, k_{ex}, τ_{in} and τ_{ex} are indicated for clarity only in the pre-injection panel. (For interpretation of the references to colour in this figure legend, the reader is referred to the Web version of this article.)

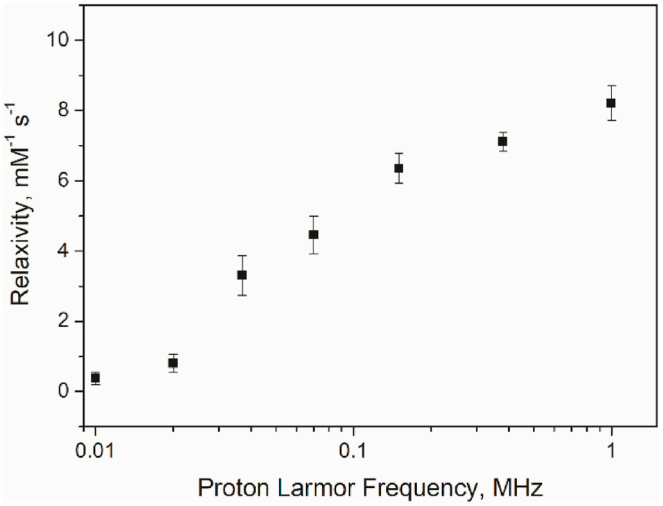

Fig. 12. The millimolar relaxivities (mM^{-1} s^{-1}) of ferumoxytol (24 h post injection) obtained by analyzing the M_z recovery curve acquired as a function of the magnetic field strength according to the 2SX model (n = 6, $[Fe]_{in}^{24h} \geq 0.2$ mM). In the fitting procedure, the ferumoxytol contribution to the relaxivity was assigned to the intra-cellular compartment. The error bars represent the Standard Errors.

because the paramagnetic contribution to relaxation rate did only increase R_{1in} and the intracellular compartment was consistently the one characterized by the fastest relaxation rates over all the observed magnetic fields range (0.01–1 MHz).

Then, by fixing R_{1in}, R_{1ex}, V_{ex} and τ_{in} at the values determined above in the absence of any added ferumoxytol, the profiles acquired 24 h after ferumoxytol injection were analysed according to 2SX model with the aim of assessing the millimolar relaxivity (in mM^{-1} s^{-1}) of intracellular ferumoxytol. The ferumoxytol contribution was added to the relaxivity of the intracellular compartment (the fast-relaxing compartment) due to the uptake of iron oxide particles by TAM, as described in the literature [10] and demonstrated above by Perls staining. The iron concentration was calculated from the T_1 measurement performed at 7 T (Fig. 4), as described above. Thus, by carrying out the 2SX analysis of the M_z evolution, it was possible, for the first time to our knowledge, to calculate the intracellular relaxivity of a superparamagnetic particle such as ferumoxytol *in vivo* on a tumour animal model. Interestingly, the curves obtained by plotting r_1 against the applied magnetic field strength (Fig. 12) showed an overall shape that appeared completely different with respect to those obtained from ferumoxytol in water, buffer and matrigel, as shown in Fig. 1. In fact, the relaxation rates displayed a kind of profile reminiscent of the one found from ferumoxytol-labelled J774A.1 macrophages. These extrapolated R_{1in} profiles shape (Fig. 12) confirmed the intra-organelles localization as surmised from the less rigorous monoexponential analysis of M_z decay reported in the previous paragraph.

4. Conclusions

From these results, one can conclude that the characteristics of the NMRD profile immediately reports on the intra- or extra-cellular localization of the contrast agent investigated (ferumoxytol). This information could not be obtained from measurements at a single magnetic field and opens new horizons for the field of cell-tracking applications. From R_1 measurements acquired before and after ferumoxytol injection it was possible to obtain a good estimation of the fraction of TAM in the tissues, a fundamental parameter for tumour characterization and treatment selection, despite the lack of spatial resolution of the prototype FFC-NMR instrumentation used in this work. Low-field FFC has recently been demonstrated as a possible technology for application in dedicated MRI scanners [21] thus supporting the view that new biomarkers, such us the intracellular water residence time, may be added to the armory of *in vivo* imaging parametres.

Declaration of competing interest

The authors declare no conflict of interest.

Acknowledgements

The authors would like to acknowledge Dr Dana Dawson, University of Aberdeen, UK, for the supply of ferumoxytol.

This project has received funding from the European Union Horizon 2020 research and innovation programme under grant agreement No 668119 (project "IDentIFY") and it was performed in the frame of the COST Action AC15209 (EURELAX). Maria Rosaria Ruggiero was supported by a "FIRC-AIRC fellowship for Italy". The Italian Ministry for Education and Research (MIUR) is gratefully acknowledged for yearly FOE funding to the Euro-BioImaging Multi-Modal Molecular Imaging Italian Node (MMMI).

Appendix A. Supplementary data

Supplementary data to this article can be found online at https://doi.org/10.1016/j.biomaterials.2020.119805.

Data availability

All data analysed during this study are included in this published article (and its supplementary information file). Other raw data required to reproduce these findings are available from the corresponding author on reasonable request.

References

[1] D. Hanahan, R.A. Weinberg, Hallmarks of cancer: the next generation, Cell 144 (2011) 646–674.
[2] R. Noy, J.W. Pollard, Tumour-associated macrophages: from mechanisms to therapy *Immunity*, 41 (2014) 49–61.
[3] S.M. Pyonteck, L. Akkari, A.J. Schuhmacher, R.L. Bowman, L. Sevenich, D.F. Quail, O.C. Olson, M.L. Quick, j.T. Huse, V. Teijeiro, M. Setty, C.S. Leslie, Y. Oei, A. Pedraza, J. Zhang, C.W. Brennan, J.C. Sutton, E.C. Holland, D. Daniel, J.A. Joyce, CSF-1R inhibition alters macrophage polarization and blocks glioma progression, Nat. Med. 19 (2013) 1264–1272.
[4] S. Sarkar, A. Döring, F.J. Zemp, C. Silva, X. Lun, X. Wang, J. Kelly, W. Hader, M. Hamilton, P. Mercier, J.F. Dunn, D. Kinniburgh, N. van Rooijen, S. Robbins, P. Forsyth, G. Cairncross, S. Weiss, V.W. Yong, Therapeutic activation of macrophages and microglia to suppress brain tumour-initiating cells, Nat. Neurosci. 17 (2013) 46–55.
[5] F.T. Andóna, E. Digifico, A. Maeda, M. Errenia, A. Mantovani, M.G. Alonso, P. Allavena, Targeting tumour associated macrophages: the new challenge for nanomedicine, Semin. Immunol. 34 (2017) 103–113.
[6] R. Yang, S. Sarkar, V.W. Yong, J.F. Dunn, In vivo MR imaging of tumour-associated macrophages: the next frontier in cancer imaging, Magn. Reson. Insights 11 (2018) 1–8.
[7] H.E. Daldrup-Link, D. Golovko, B. Ruffell, D.G. DeNardo, R. Castaneda, C. Ansari, J. Rao, G.A. Tikhomirov, M.F. Wendland, C. Corot, L.M. Coussens, MRI of tumor-associated macrophages with clinically applicable iron oxide nanoparticles, Clin. Canc. Res. 17 (2011) 5695–5704.
[8] A.V. Makela, J.M. Gaudet, P.J. Foster, Quantifying tumor associated macrophages in breast cancer: a comparison of iron and fluorinebased MRI cell tracking, Sci. Rep. 7 (2017) 42109.
[9] S. Laurent, J.L. Bridot, L. Vander Elst, R.N. Muller, Magnetic iron oxide nanoparticles for biomedical applications *Future*, Med. Chem. 2 (2010) 427–449.
[10] M. Aghighi, A.J. Theruvath, A. Pareek, L.L. Pisani, R. Alford, A.M. Muehe, T.K. Sethi, S.J. Holdsworth, F.K. Hazard, D. Gratzinger, S. Luna-Fineman, R. Advani, S.L. Spunt, H.E. Daldrup-Link, Magnetic resonance imaging of tumor-associated macrophages: clinical translation, Clin. Canc. Res. 24 (2018) 4110–4118.
[11] J.W.M. Bulte, H.E. Daldrup-Link, Clinical tracking of cell transfer and cell transplantation: trials and tribulations, Radiology 289 (2018) 604–615.
[12] S.M. Cromer Berman, P. Walczak, J.W.M. Bulte, Tracking stem cells using magnetic nanoparticles Tracking stem cells using magnetic nanoparticles, Wiley Interdiscip. Rev. Nanomed. Nanobiotechnol. 3 (2011) 343–355.
[13] M. Lu, M.H. Cohen, D. Rieves, R. Pazdur, FDA report: ferumoxytol for intravenous iron therapy in adult patients with chronic kidney disease, Am. J. Hematol. 85 (2010) 315–319.
[14] J.P. Bullivant, S. Zhao, B.J. Willenberg, B. Kozissnik, C.D. Batich, J. Dobson, Materials characterization of feraheme/ferumoxytol and preliminary evaluation of its potential for magnetic fluid hyperthermia, Int. J. Mol. Sci. 14 (2013) 17501–17510.
[15] P.L. McCormack, Ferumoxytol, In iron deficiency anaemia in adults with chronic kidney disease, Drugs 72 (2012) 2013–2022.
[16] M.F. Attia, N. Anton, J. Wallyn, Z. Omran, T.F. Vandamme, An overview of active and passive targeting strategies to improve the nanocarriers efficiency to tumour sites, J. Pharm. Pharmacol. 71 (2019), https://doi.org/10.1111/jphp.13098.
[17] S.M. Dadfar, K. Roemhild, N.I. Drude, S. von Stillfried, R. Knüchel, F. Kiessling, T. Lammers, Iron oxide nanoparticles: diagnostic, therapeutic and theranostic applications, Adv. Drug Deliv. Rev. 138 (2019) 302–325.
[18] R. Weissleder, M. Nahrendorf, M.J. Pittet, Imaging macrophages with nanoparticles, Nat. Mater. 13 (2014) 125–138.
[19] M.R. Bashir, L. Bhatti, D. Marin, R.C. Nelson, Emerging applications for ferumoxytol as a contrast agent in MRI, JMRI 41 (2015) 884–898.
[20] S.R. Alam, G.H. Tse, C. Stirrat, T.J. MacGillivray, R.J. Lennen, M.A. Jansen, D.E. Newby, L. Marson, P.A. Henriksen, Nanoparticle enhanced MRI scanning to detect cellular inflammation in experimental chronic renal allograft rejection, Int. J. Mol. Imaging (2015) 8, https://doi.org/10.1155/2015/507909 Article ID 507909.
[21] J. Budjan, S. Neudecker, D. Schock-Kusch, B. Kraenzlin, S.O. Schoenberg, H.J. Michaely, U.I. Attenberger, Can ferumoxytol be used as a contrast agent to differentiate between acute and chronic inflammatory kidney disease?: feasibility study in a rat model, Invest. Radiol. 51 (2016) 100–105.
[22] M. Aghighi, D. Golovko, C. Ansari, N.M. Marina, L. Pisani, L. Kurlander, C. Klenk, S. Bhaumik, M. Wendland, H.E. Daldrup-Link, Imaging tumor necrosis with ferumoxytol, PloS One 10 (2015) e0142665.
[23] H. Alsaid, T. Skedzielewski, M.V. Rambo, K. Hunsinger, B. Hoang, W. Fieles, E.R. Long, J. Tunstead, D.J. Vugts, M. Cleveland, N. Clarke, C. Matheny, B.M. Jucker, Non invasive imaging assessment of the biodistribution of GSK2849330, an ADCC and CDC optimized anti HER3 mAb, and its role in tumor macrophage recruitment in human tumor-bearing mice, PloS One 12 (2017) e0176075.
[24] M.R. Ruggiero, S. Baroni, S. Pezzana, G. Ferrante, S. Geninatti Crich, S. Aime, Evidence for the role of intracellular water lifetime as a tumour biomarker obtained by In Vivo field-cycling relaxometry, Angew. Chem. 57 (2018) 7468–7472.
[25] S. Baroni, M.R. Ruggiero, S. Aime, S. Geninatti Crich, Exploring the tumour extracellular matrix by in vivo Fast Field Cycling relaxometry after the administration of a Gadolinium-based MRI contrast agent, Magn. Reson. Chem. 57 (2019) 845–851, https://doi.org/10.1002/mrc.4837.
[26] Y.T. Araya, F. Martínez-Santiesteban, W.B. Handler, C.T. Harris, B.A. Chronik, T.J. Scholl, Nuclear magnetic relaxation dispersion of murine tissue for development of T_1 (R_1) dispersion contrast imaging, NMR Biomed. 30 (2017) e3789.
[27] L.M. Broche, P.J. Ross, G.R. Davies, M.J. MacLeod, D.J. Lurie, A whole-body Fast Field-Cycling scanner for clinical molecular imaging studies, Sci. Rep. 9 (9) (2019), https://doi.org/10.1038/s41598-019-46648-0 Article number: 10402.
[28] L.M. Broche, G.P. Ashcroft, D.J. Lurie, Detection of osteoarthritis in knee and hip joints by fast field-cycling, Magn. Reson. Med. 68 (2012) 358–362.
[29] P.J. Ross, L.M. Broche, D.J. Lurie, Rapid field-cycling MRI using fast spin-echo, Magn. Reson. Med. 73 (2015) 1120–1124.
[30] G.J. Gage, D.R. Kipke, W. Shain, Whole animal perfusion fixation for rodents whole animal perfusion fixation for rodents, JoVE 65 (2012) e3564.
[31] X. Li, S. Mangia, J.H. Lee, R. Bai, C.S. Springer Jr., NMR shutter-speed elucidates apparent population inversion of ^1H_2O signals due to active transmembrane water cycling, Magn. Reson. Med. (2019) 1–14.
[32] C.S. Springer Jr., Using ^1H_2O MR to measure and map sodium pump activity in vivo, J. Magn. Reson. 291 (2018) 110–126.
[33] C.S. Landis, X. Li, F.W. Telang, P.E. Molina, I. Palyka, G. Vetek, C.S. Springer Jr., Equilibrium transcytolemmal water-exchange kinetics in skeletal muscle in vivo, Magn. Reson. Med. 42 (1999) 467–478.
[34] C.S. Springer Jr., X. Li, L.A. Tudorica, K.Y. Oh, N. Roy, S.Y. Chui, A.M. Naik, M.L. Holtorf, A. Afzal, W.D. Rooney, W. Huang, Intratumor mapping of intracellular water lifetime: metabolic images of breast cancer? NMR Biomed. 27 (2014) 760–773.
[35] E. Panagiotaki, S. Walker-Samuel, B. Siow, S.P. Johnson, V. Rajkumar, R.B. Pedley, M.F. Lythgoe, D.C. Alexander, Noninvasive quantification of solid tumor microstructure using VERDICT MRI, Cancer Res 74 (2014) 1902–1912.
[36] X. Li, W. Huang, E.A. Morris, L.A. Tudorica, V.E. Seshan, W.D. Rooney, I. Tagge, Y. Wang, J. Xu, C.S. Springer Jr., Dynamic NMR effects in breast cancer dynamic-contrast-enhanced MRI, Proc. Natl. Acad. Sci. Unit. States Am. 105 (2008) 17937–17942.
[37] S.L. Barnes, A.G. Sorace, M.E. Loveless, J.G. Whisenant, T.E. Yankeelov, Correlation of tumor characteristics derived from DCE-MRI and DW-MRI with histology in murine models of breast cancer, NMR Biomed. 28 (2015) 1345–1356.
[38] C.S. Landis, X. Li, V. Telang, J.A. Coderre, P.L. Micca, W.D. Rooney, L.L. Latour, G. Vétek, I. Pályka, C.S. Springer Jr., Determination of the MRI contrast agent concentration time course in vivo following bolus injection: effect of equilibrium transcytolemmal water exchange, Magn. Reson. Med. 44 (2000) 563–574.
[39] U. Del Monte, Does the cell number 10(9) still really fit one gram of tumor tissue? Cell Cycle 8 (2009) 505–506.
[40] C.S. Hughes, L.M. Postovit, G.A. Lajoie, Matrigel: a complex protein mixture required for optimal growth of cell culture, Proteomics 10 (2010) 1886–1890.
[41] L. Bordonali, T. Kalaivani, K.P. Sabareesh, C. Innocenti, E. Fantechi, C. Sangregorio, M.F. Casula, L. Lartigue, J. Larionova, Y. Guari, M. Corti, P. Arosio, A. Lascialfari, NMR-D study of the local spin dynamics and magnetic anisotropy in different nearly monodispersed ferrite nanoparticles, J. Phys. Condens. Matter 25 (2013) 066008.
[42] S. Laurent, D. Forge, M. Port, A. Roch, C. Robic, L. Vander Elst, R.N. Muller, Magnetic iron oxide nanoparticles: synthesis, stabilization, vectorization, physicochemical characterizations, and biological applications, Chem. Rev. 108 (2008) 2064–2110.
[43] M.R. Ruggiero, S. Geninatti Crich, E. Sieni, P. Sgarbossa, M. Forzan, E. Cavallari, R. Stefania, F. Dughiero, S. Aime, Magnetic hyperthermia efficiency and 1H-NMR relaxation properties of iron oxide/paclitaxel-loaded PLGA nanoparticles, Nanotechnology 27 (2016) 285104.
[44] A. Roch, R.N. Muller, P. Gillis, Theory of proton relaxation induced by superparamagnetic particles, J. Chem. Phys. 110 (1999) 5403–5411.
[45] S.L. Rego, R.S. Helms, D. Dréau, Breast tumor cell TACE-shed MCSF promotes pro-angiogenic macrophages through NF-κB signaling, Angiogenesis 17 (2014) 573–585.
[46] E. Terreno, S. Geninatti Crich, S. Belfiore, L. Biancone, C. Cabella, G. Esposito, A.D. Manazza, S. Aime, Effect of the intracellular localization of a Gd-based imaging

probe on the relaxation enhancement of water protons, Magn. Reson. Med. 55 (2006) 491–497.
[47] G.J. Strijkers, S. Hak, M.B. Kok, C.S. Springer, K. Nicolay, Three-compartment T1 relaxation model for intracellular paramagnetic contrast agents, Magn. Reson. Med. 61 (2009) 1049–1058.
[48] M.B. Kok, S. Hak, W.J.M. Mulder, D.W.J. van der Schaft, G.J. Strijkers, K. Nicolay, Cellular compartmentalization of internalized paramagnetic liposomes strongly influences both T1 and T2 relaxivity, Magn. Reson. Med. 61 (2009) 1022–1032.
[49] E. Gianolio, G. Ferrauto, E. Di Gregorio, S. Aime, Re-evaluation of the water exchange lifetime value across red blood cell membrane, Biochim. Biophys. Acta 1858 (2016) 627–631.
[50] G. Jarockyte, E. Daugelaite, M. Stasys, U. Statkute, V. Poderys, T.C. Tseng, S.H. Hsu, V. Karabanovas, R. Rotomskis, Accumulation and toxicity of superparamagnetic iron oxide nanoparticles in cells and experimental animals, Int. J. Mol. Sci. 19 (17) (2016) 1193.
[51] H. Wang, L. Yang, D. Wang, Q. Zhang, L. Zhang, Pro-tumor activities of macrophages in the progression of melanoma, Hum. Vaccines Immunother. 7 (2017) 1556–1562.
[52] M. Pieniazek, R. Matkowski, P. Donizy, Macrophages in skin melanoma-the key element in melanomagenesis, Oncol Lett 4 (2018) 5399–5404.
[53] M. Mrad, C. Imbert, V. Garcia, F. Rambow, N. Therville, S. Carpentier, B. Ségui, T. Levade, R. Azar, J.C. Marine, M. Diab-Assaf, C. Colacios, N. Andrieu-Abadie, Downregulation of sphingosine kinase-1 induces protective tumor immunity by promoting M1 macrophage response in melanoma, Oncotarget 7 (2016) 71873–71886.
[54] M. Iv, P. Samghabadi, S. Holdsworth, A. Gentles, P. Rezaii, G. Harsh, G. Li, R. Thomas, M. Moseley, H.E. Daldrup-Link, H. Vogel, M. Wintermark, S. Cheshier, K.W. Yeom, Quantification of macrophages in high-grade gliomas by using ferumoxytol-enhanced MRI: a Pilot study, Radiology 290 (2019) 198–206.
[55] M.A. Miller, S. Arlauckas, R. Weissleder, Prediction of anti-cancer nanotherapy efficacy by imaging, Nanotheranostics 1 (2017) 296–312.
[56] J. Du, V. Sheth, Q. He, M. Carl, J. Chen, J. Corey-Bloom, G.M. Bydder, Measurement of T1 of the ultrashort T2* components in white matter of the brain at 3T, PloS One 9 (2014) e103296.
[57] M.R. Hussein, Tumour-associated macrophages and melanoma tumourigenesis: integrating the complexity, Int. J. Exp. Pathol. 87 (2006) 163–176.
[58] L. Donofrio, G. Tebaldi, S. Lanzardo, R. Ruiu, E. Bolli, A. Ballatore, V. Rolih, F. Macchi, L. Conti, F. Cavallo, Bovine herpesvirus 4-based vector delivering the full length xCT DNA efficiently protects mice from mammary cancer metastases by targeting cancer stem cells, OncoImmunology 7 (12) (2018) e1494108.
[59] D. Giavarina, Understanding Bland altman analysis, Biochem. Med. 25 (2015) 141–151.
[60] S.K. Hanneman, Design, analysis and interpretation of method-comparison studies, AACN Adv. Crit. Care 19 (2008) 223–234.
[61] H.E. Daldrup-Link, L.M. Coussens, MR imaging of tumor-associated macrophages, OncoImmunology 1 (2012) 507–509.
[62] Q. Cao, X. Yan, K. Chen, Q. Huang, M.P. Melancon, G. Lopez, Z. Cheng, C. Li, Macrophages as a potential tumor-microenvironment target for noninvasive imaging of early response to anticancer therapy, Biomaterials 152 (2018) 63–76.